ADVANCED INTELLIGENT SYSTEMS
Open Access
www.advintellsyst.com

A Data-Centric Approach to Quantifying the Forward and Inverse Relationship Between Laser Powder Bed Fusion Process Parameters and as-Built Surface Roughness of IN718 Parts

*Samsul Mahmood and Bart Raeymaekers**

Laser powder bed fusion (PBF-LB) is an additive manufacturing (AM) technology for producing complex geometry parts. However, the high cost of post-processing coarse as-built surfaces drives the need to control surface roughness during fabrication. Prior studies have evaluated the relationship between process parameters and as-built surface roughness, but they rely on forward models using trial-and-error, regression, and data-driven methods based only on areal surface roughness parameters that neglect spatial surface characteristics. In contrast, this study introduces, for the first time, an inverse data-centric framework that leverages machine learning algorithms and an experimental dataset of Inconel 718 as-built surfaces to predict the PBF-LB process parameters required to achieve a desired as-built roughness. This inverse model shows a prediction accuracy of ≈80%, compared to 90% for the corresponding forward model. Additionally, it incorporates deterministic surface roughness parameters, which capture both height and spatial information, and significantly improves prediction accuracy compared to only using areal parameters. The inverse model provides a digital tool to process engineers that enables control of surface roughness by tailoring process parameters. Hence, it establishes a foundation for integrating surface roughness control into the digital thread of AM, thereby reducing the need for post-processing and improving process efficiency.

1. Introduction

Laser powder bed fusion (PBF-LB) is a widely adopted metal additive manufacturing (AM) technology capable of manufacturing high-value parts with complex internal and external geometry. The process selectively melts thin layers of metal powder using a laser, enabling precise control of part geometry.[1] PBF-LB is extensively used in the aerospace,[2–5] medical device,[6–9] and automotive industries,[10,11] where conventional manufacturing processes often limit design complexity. Despite its advantages, PBF-LB typically produces parts with coarse as-built surfaces that exhibit characteristic surface features such as the staircase effect, partially fused powder particles, and porosity.[12,13] These features originate from the layer-by-layer fabrication process and steep thermal gradients near the melt pool. Surface roughness significantly influences the mechanical properties of PBF-LB parts, particularly fatigue strength, as (sub)surface defects can serve as crack initiation sites.[14–17]

Although recent improvements in the quality of metal powders,[18,19] laser control, and scan strategies[20] have reduced porosity and as-built surface roughness, post-processing remains necessary to meet functional and dimensional specifications prior to placing parts into service. Moreover, internal geometries often remain inaccessible to post-processing, potentially creating critical stress concentrations or failure sites. Hence, several post-processing techniques have been used to modify the as-built surface roughness. Machining and superfinishing remove material,[21,22] whereas hot isostatic pressing[23–25] and annealing[26] use pressure and temperature to decrease porosity and surface roughness. Additionally, chemical treatment[27] removes partially fused powder particles, and other methods, such as shot peening, utilize mechanical impact to reduce as-built surface roughness.[28,29] However, these processes are time-intensive and costly, limiting the economic viability of PBF-LB for serial production.

Eliminating post-processing by directly controlling or tailoring surface roughness during fabrication would significantly reduce cost and increase throughput, transforming PBF-LB into a viable production technology. This approach requires quantifying the complex, nonlinear relationships between PBF-LB process parameters and as-built surface roughness. However, conventional approaches based on trial-and-error or multivariate

S. Mahmood, B. Raeymaekers
Department of Mechanical Engineering
Virginia Tech
Blacksburg, VA 24061, USA
E-mail: bart.raeymaekers@vt.edu

The ORCID identification number(s) for the author(s) of this article can be found under https://doi.org/10.1002/aisy.202500409.

DOI: 10.1002/aisy.202500409

regression are limited in their ability to capture these interactions across the entire process envelope.[30–33]

Previous studies characterize the as-built surface roughness of parts fabricated with PBF-LB with both profile (e.g., *Ra*, *Rv*, *Rku*, *Rp*, *Rsk*) and areal surface roughness parameters (e.g., *Sa*, *Sv*, *Sp*, *Sku*, *Ssk*), which are standardized in ISO 21920[34] and ISO 25178[35] (also see a brief summary in Section 2.3). Yet, these metrics solely rely on surface height data and do not incorporate spatial information that is critical for distinguishing surface features such as pores or partially fused particle agglomerations.[12,33] Recent work has introduced deterministic surface roughness parameters, including the standard deviation of asperity heights σ_s, mean asperity radius R_s, and asperity density η_s,[36,37] which better correlate with PBF-LB process parameters and provide a more robust characterization of as-built PBF-LB surface roughness.[12]

To overcome modeling limitations and gain a detailed understanding of the process-surface relationship, researchers have adopted data-centric models based on machine learning (ML) algorithms to predict as-built surface roughness from PBF-LB process parameters.[38–42] These forward models, typically based on artificial neural networks (ANNs),[39,43–47] random forests (RF),[46] support vector regression (SVR),[40,46] and extreme gradient boosting (XGBoost),[48] achieve a prediction accuracy in excess of 90%. This is particularly true when incorporating process parameters such as scan strategy and raster pattern,[43–45] or deterministic surface roughness parameters,[12,38] alongside more conventional inputs such as laser power and laser scan speed. Nevertheless, these models often rely on sparse or synthetic datasets, do not consider important parameters like build orientation,[47] which is known to have a strong effect on surface roughness,[12] and primarily predict average surface roughness *Sa*, offering limited insight into local surface roughness results.[48]

Volumetric energy density (VED), in addition to laser power, is also commonly used to characterize the PBF-LB process. However, VED does not correlate strongly with the as-built surface roughness parameters because similar surface roughness arises from different VED values.[49] More advanced metrics such as dimensionless heat input[50] or hybrid datasets blending experimental and synthetic data[51,52] have improved model generalization, and optimization frameworks (e.g., Kriging[53]) have emerged to improve prediction accuracy. Alternatively, supplementing experiments with synthetic surface roughness data increases the available dataset to improve the prediction accuracy of data-centric models.

Despite this progress, three critical knowledge gaps remain unaddressed. First, areal surface roughness parameters insufficiently capture local surface features and show weak correlation with PBF-LB process parameters because they do not consider spatial in addition to height information. Second, existing models often focus on narrow subsets of the process envelope due to the cost of experiments or application-specific constraints. Third, existing publications document forward data-centric models, predicting as-built surface roughness (output) from PBF-LB process parameters (input). However, inverse models, which predict PBF-LB process parameters (output) required to achieve a specific as-built surface roughness (input), have not yet been presented. Yet, inverse models are essential to enabling intelligent process control, whereby users can specify a desired surface roughness and obtain the required PBF-LB process parameters to realize it in situ, without additional post-processing.

Thus, this work introduces the first framework for inverse data-centric modeling of PBF-LB as-built surface roughness, using experimentally acquired surface data for Inconel 718 (IN718) across the full process envelope. We derive both forward and inverse data-centric models that incorporate areal, deterministic, and hybrid surface roughness parameters to evaluate prediction accuracy and inform PBF-LB process tuning. Notably, we demonstrate that deterministic surface roughness parameters, which capture both height and spatial information, substantially increase model prediction accuracy. This approach enables the implementation of a digital process twin that facilitates the prediction, visualization, and inverse design of tailored surface roughness during fabrication. Hence, this work establishes a foundation for embedding surface roughness control into the digital thread of AM, offering a pathway to reduce post-processing, accelerate qualification, and expand the use of PBF-LB from prototyping to production.

2. Experimental Section

2.1. AM of Specimens

Sixteen truncheon specimens are fabricated using IN718 powder (26 μm average diameter) and an EOS M290 PBF-LB printer, consistent with previous work from our group.[12] Since this work focuses on the as-built surface roughness, the contour laser process parameters used to fabricate each of the 16 specimens are varied, while a constant 40 μm layer thickness, a 15 μm hatch offset, and the EOS-recommended interior hatching process parameters for IN718 are maintained.

Figure 1a shows a schematic of a truncheon specimen with 19 different $25 \times 25 \times 4$ mm square sections of build orientation $0° \leq \alpha \leq 90°$ (5° increments). Figure 1b shows a photograph of a representative truncheon specimen, whereas Figure 1c depicts a cutaway view to illustrate the interior hatching pattern of the specimen, and the contour 2 (outermost, red line) and contour 1 (innermost, blue line) laser passes that aim to smooth the as-built surface roughness (similar to laser polishing).[54] When both contour laser passes apply, contour 1 precedes contour 2 with a constant 12 μm offset. When a single contour laser pass applies, contour 1 is not used. Figure 1d schematically shows the layout of the truncheon specimens on the build plate with respect to the build-, recoater-, and gas flow directions. The spatial layout of the specimens is selected to minimize variations due to local thermal or flow field effects during fabrication. A build plate fits eight truncheon specimens and requires ≈40 h to print.

Table 1 summarizes the PBF-LB contour laser parameters used to fabricate each of the 16 truncheon specimens. Specimens 1–6 use down-skin settings, whereas specimens 7–16 use up-skin settings. Importantly, the PBF-LB process parameters are maintained constant for each truncheon specimen, regardless of whether a surface corresponds to an up-skin or down-skin condition. To investigate the influence of process parameters on as-built surface roughness, the contour laser power P and laser scan speed v are systematically varied by

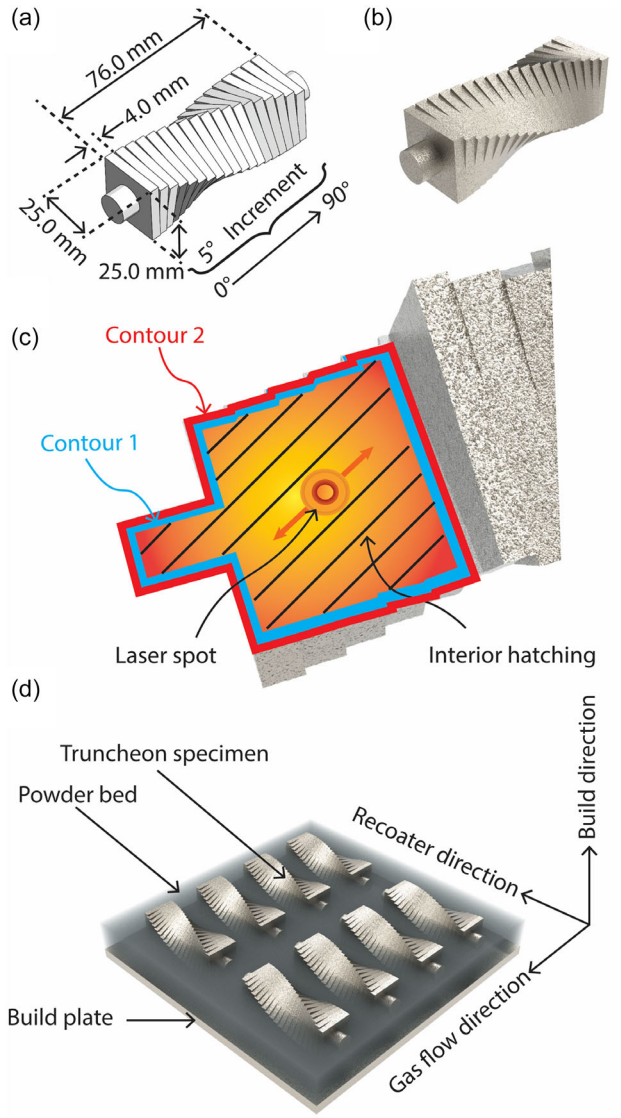

Figure 1. a) Geometry and dimensions of the truncheon specimen. b) Photograph of a representative specimen, and c) a cutaway view that illustrates the interior hatching and contour laser passes. d) Schematic that shows the location of the specimens on the build plate with respect to the process directions.

$\approx \pm 10\%$ and $\pm 20\%$ around the EOS-recommended parameters for IN718, which are $P = 35$ W and $v = 2{,}000$ mm s^{-1} (contour 2 only) and $P = 138$ W and $v = 390$ mm s^{-1}, and $P = 80$ W at $v = 800$ mm s^{-1} (contour 1 and contour 2), respectively. Changing process parameters beyond $\pm 20\%$ risks insufficient fusion of metal powder particles or melt pool overheating.[55,56] To assess process repeatability across different build plates, the process parameters for specimens 2 and 5, and 9 and 14 are duplicated. Furthermore, the contour laser power is varied while maintaining constant laser scan speed to fabricate specimens 7–11, whereas the laser scan speed is varied while maintaining constant laser power to fabricate specimens 12–16. Hence, this systematic design of the experiments enables evaluation of both individual and combined effects of PBF-LB process parameters on the resulting as-built surface roughness, covering the entire process envelope.

2.2. Surface Roughness Measurement

Measuring surface roughness involves quantifying and mapping the surface height z at discrete coordinate locations (x,y), i.e., $z = f(x,y)$. Here, surface height data is collected using a white light interferometer (Contour X-500, Bruker, Tucson, AZ) with a 10× objective lens. The setup provides a field-of-view of 1200×1000 pixels with 0.38 µm lateral resolution and 1–5 nm vertical resolution.[12] All measurements are corrected for specimen tilt to ensure consistency across surfaces.

To capture the surface features typical of PBF-LB, nine individual surface roughness measurements are stitched together, resulting in a 1.8×1.8 mm surface roughness map. The measurement parameters and protocol are established based on a convergence study to ensure that the surface roughness results are independent of measurement resolution and field-of-view. To improve data fidelity, a Gaussian regression filter is applied to minimize measurement noise, and a neighborhood averaging method is employed to restore up to 5% missing pixel data, both caused by the limited light reflectivity of the coarse as-built surfaces.

Figure 2a schematically illustrates the measurement region of the as-built surface roughness on each square of the truncheon specimens (center of each individual square). The up-skin surfaces (build orientation $\alpha = 5°$ to $85°$ relative to the build direction), the top surface ($\alpha = 0°$), and the side surface ($\alpha = 90°$) are included. Down-skin surfaces are excluded from the analysis, as support structure removal would compromise their as-built condition. Figure 2b presents representative roughness maps of specimen 02 ($\alpha = 70°$) and specimen 03 ($\alpha = 5°$), highlighting typical surface features that result from PBF-LB, including pores, balling, interior hatching patterns, contour laser scan lines, staircase effect, and partially fused powder particles.

2.3. Quantifying As-Built Surface Roughness

As-built surfaces are characterized using areal, deterministic, and hybrid surface roughness parameters. Areal surface roughness parameters include average surface roughness *Sa*, root mean square (RMS) roughness *Sq*, skewness *Ssk*, and kurtosis *Sku* (see ISO 25178).[35] Skewness *Ssk* indicates the relative presence of peaks and valleys, where $Ssk > 0$ indicates more peaks than valleys and $Ssk < 0$ indicates the opposite. Kurtosis *Sku* measures surface sharpness, with $Sku > 3$ denoting sharp peaks and $Sku < 3$ indicating rounded peaks.

Deterministic surface roughness parameters are derived from surface peak statistics and include the standard deviation of asperity heights σ_s, mean asperity radius R_s, and the asperity density η_s. First, all peaks on the surface are identified using an eight-nearest neighbor algorithm. Parameter σ_s is computed directly from the peak heights, whereas η_s represents the number of peaks per unit area. The mean asperity radius R_s is calculated as the mean of all peak radii $R_{s,i} = -[(\kappa_{x,i} + \kappa_{y,i})/2]^{-1}$, with $\kappa_{x,i} = d^2z/dx^2$ and $\kappa_{y,i} = d^2z/dy^2$, respectively.[36,37] Note that the roughness parameter σ_s/R_s is a dimensionless metric for surface roughness.

Table 1. PBF-LB process parameters for each specimen, including contour laser power P and scan speed v, LED (based on scan speed only), and VED (based on scan speed and layer thickness).

Specimen	Contour 1				Contour 2			
	Laser power P_1 [W]	Scan speed v_1 [mm s^{-1}]	Laser energy density		Laser power P_2 [W]	Scan speed v_2 [mm s^{-1}]	Laser energy density	
			Linear [Ws mm^{-1}]	Volume [Ws mm^{-2}]			Linear [Ws mm^{-1}]	Volume [Ws mm^{-2}]
1	0.0	4000.0	0.000	0.000	28.0	2000.0	0.014	0.350
2	0.0	4000.0	0.000	0.000	35.0	2000.0	0.018	0.438
3	0.0	4000.0	0.000	0.000	42.0	2000.0	0.021	0.525
4	0.0	4000.0	0.000	0.000	35.0	1666.7	0.021	0.525
5	0.0	4000.0	0.000	0.000	35.0	2000.0	0.018	0.438
6	0.0	4000.0	0.000	0.000	35.0	2500.0	0.014	0.350
7	110.4	390.0	0.283	7.077	64.0	800.0	0.080	2.000
8	124.2	390.0	0.318	7.962	72.0	800.0	0.090	2.250
9	138.0	390.0	0.354	8.846	80.0	800.0	0.100	2.500
10	151.8	390.0	0.389	9.731	88.0	800.0	0.110	2.750
11	165.6	390.0	0.425	10.615	96.0	800.0	0.120	3.000
12	138.0	487.5	0.283	7.077	80.0	1000.0	0.080	2.000
13	138.0	433.3	0.318	7.962	80.0	888.9	0.090	2.250
14	138.0	390.0	0.354	8.846	80.0	800.0	0.100	2.500
15	138.0	354.5	0.389	9.731	80.0	727.3	0.110	2.750
16	138.0	325.0	0.425	10.615	80.0	666.7	0.120	3.000

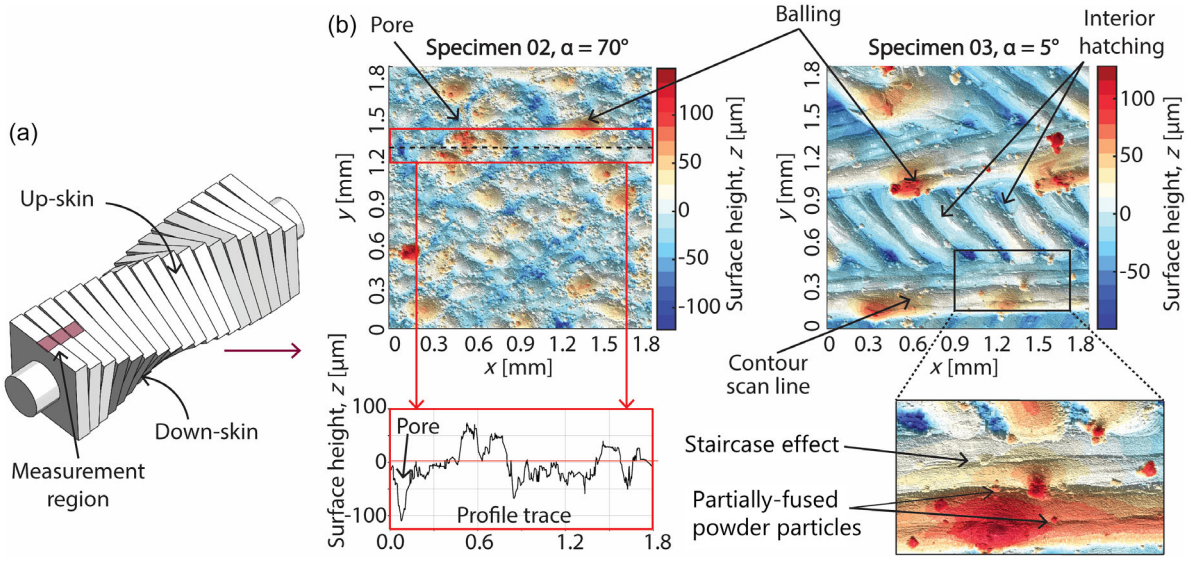

Figure 2. a) Schematic indicating the locations where the as-built surface roughness on the truncheon specimens is measured (center of each square). b) Surface roughness maps of specimen 02 ($\alpha = 70°$) and specimen 03 ($\alpha = 5°$), identify characteristic features of as-built PBF-LB surfaces.

Hybrid surface roughness parameters derive from the surface height and the primary spatial wavelength and include the RMS surface slope *Sdq* and the developed interfacial area ratio *Sdr* (see ISO 25 178).[35] These parameters are specifically useful to distinguish between surfaces with similar *Sa* yet qualitatively different surface features.[57]

2.4. Data-Centric Models Based on ML Algorithms

2.4.1. Forward Data-Centric Model

Figure 3 presents a schematic overview of the methodology used to develop and validate forward data-centric models that predict

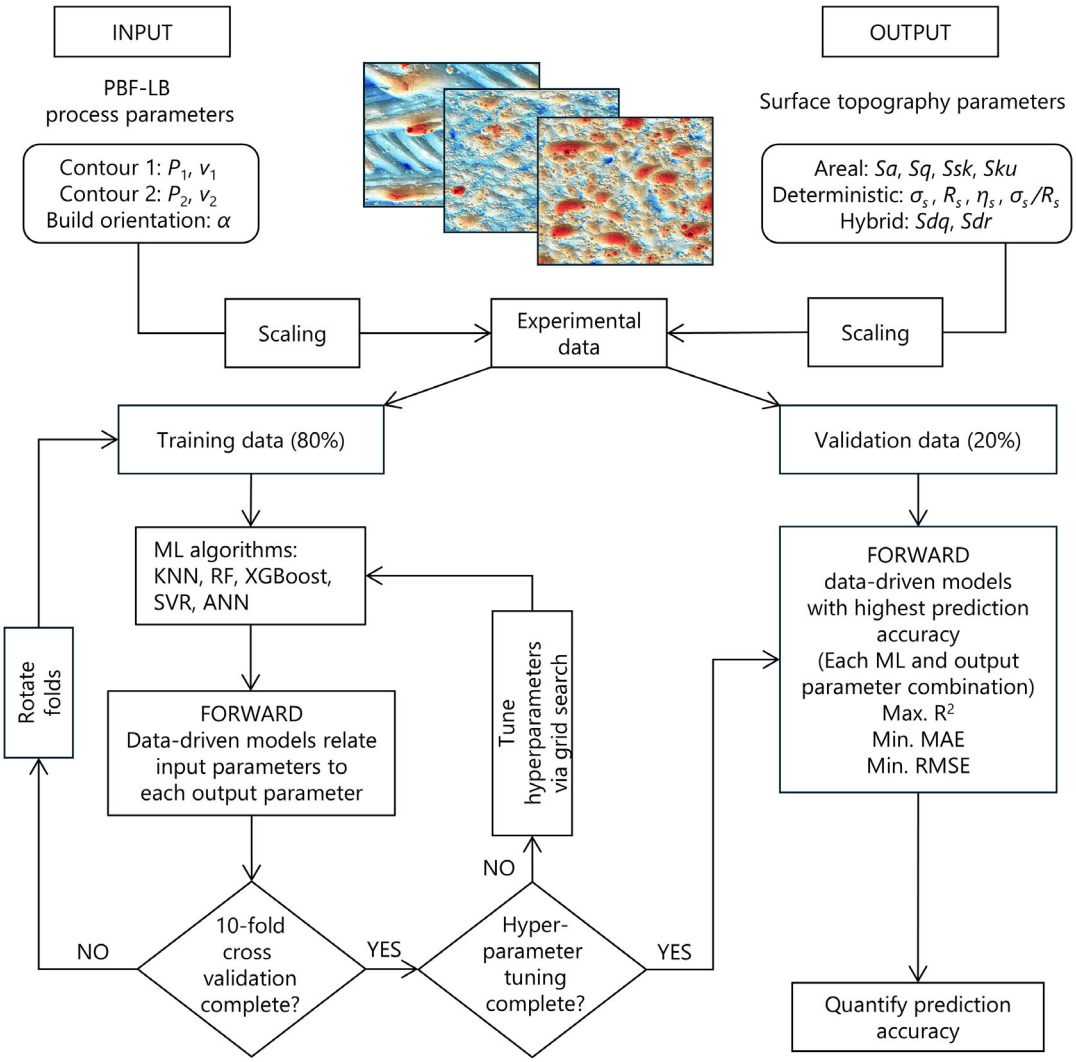

Figure 3. Flowchart of the methodology to develop and validate forward data-centric models that link the PBF-LB process parameters (input) to the as-built surface roughness parameters (output).

the as-built surface roughness parameters (output) from PBF-LB process parameters (input). The models consider five PBF-LB process parameters as input: laser power and laser scan speed of the contour 1 and 2 laser passes, i.e., P_1, v_1, P_2, v_2, and the build orientation α. The volume energy density (VED) and linear energy density (LED) are deliberately not included as additional process parameters (input) in the models to prevent overfitting since they are a function of P_1, v_1, P_2, and v_2. Although commonly used in the literature, VED and LED are non-unique process parameters because multiple combinations of laser power and scan speed can yield identical values, thus limiting their predictive capability. Only using LED and VED as process parameters (input) did not result in models with high prediction accuracy.

The models consider areal (*Sa*, *Sq*, *Ssk*, *Sku*), deterministic (σ_s, R_s, η_s, σ_s/R_s), and hybrid (*Sdq*, *Sdr*) surface roughness parameters (output). To normalize differences in unit scale, magnitude, and range across the process parameters, *z*-score normalization is applied.[58] The dataset is split randomly into 80% for model training and 20% for independent model validation. To construct data-centric models, three interpretable ML algorithms are used: *k*-nearest neighbors (KNN), RF, XGBoost, and two non-interpretable algorithms: SVR and ANN. Mathematical descriptions of these algorithms are available elsewhere (see e.g., Toorandaz et al. and Burkov),[48,59] and are omitted here for brevity.

Prediction accuracy of each data-centric model is evaluated using the coefficient of determination (R^2), the mean absolute error (MAE), and the RMS error (RMSE).[60] Prediction accuracy of each model is iteratively optimized via hyperparameter tuning using a grid search strategy, iteratively adjusting algorithm-specific parameters to maximize R^2 while minimizing MAE and RMSE. To further improve the prediction accuracy of the models, tenfold cross-validation is applied;[59] the training data is split into ten random folds, where nine folds are used to train the models and the remaining fold serves as a validation set. This

process is repeated ten times until each fold serves as a validation set exactly once.

In total, 50 data-centric models are constructed (one for each combination of five ML algorithms and ten surface roughness parameters), each tuned to maximize prediction accuracy. Finally, the 20% hold-out validation data is used to quantify the prediction accuracy of all 50 models, again by determining R^2, MAE, and RMSE. The data-centric models with the highest prediction accuracy for each surface roughness parameter are identified.

To evaluate whether the differences in prediction accuracy between the different data-centric models are statistically significant, a non-parametric statistical analysis is performed using the Friedman test, followed by the Nemenyi post-hoc test for pairwise comparisons.[61] Each model is independently trained and evaluated five times using tenfold cross-validation with different random seeds, which results in five R^2 scores per model for each surface roughness parameter. The Friedman test assesses whether statistically significant differences exist ($p < 0.05$) between the prediction accuracy of the different data-centric models for all surface roughness parameters. If significance is detected, the Nemenyi post-hoc test is used to conduct pairwise comparisons and identify which model pairs differ significantly.

2.4.2. Inverse Data-Centric Model

Figure 4 presents a schematic overview of the methodology used to develop and validate inverse data-centric models that predict the PBF-LB process parameters (output) from desired surface roughness parameters (input). In contrast to the forward model, where a user inputs well-known PBF-LB process parameters, it is not intuitive to input any number of different areal, deterministic, and hybrid surface roughness parameters that characterize a desired as-built surface roughness. Yet, without sufficient quantitative information that describes the desired as-built surface roughness, this inverse problem is inherently ill-posed, and it is not possible to predict useful PBF-LB process parameters. Hence, we adopt a two-step modeling strategy.

In step 1, the user specifies a desired as-built surface roughness by means of a single *Sa* and built orientation α. A first ANN-based model (data-centric model 1 in Figure 4) uses these inputs to predict the full set of ten surface roughness parameters,

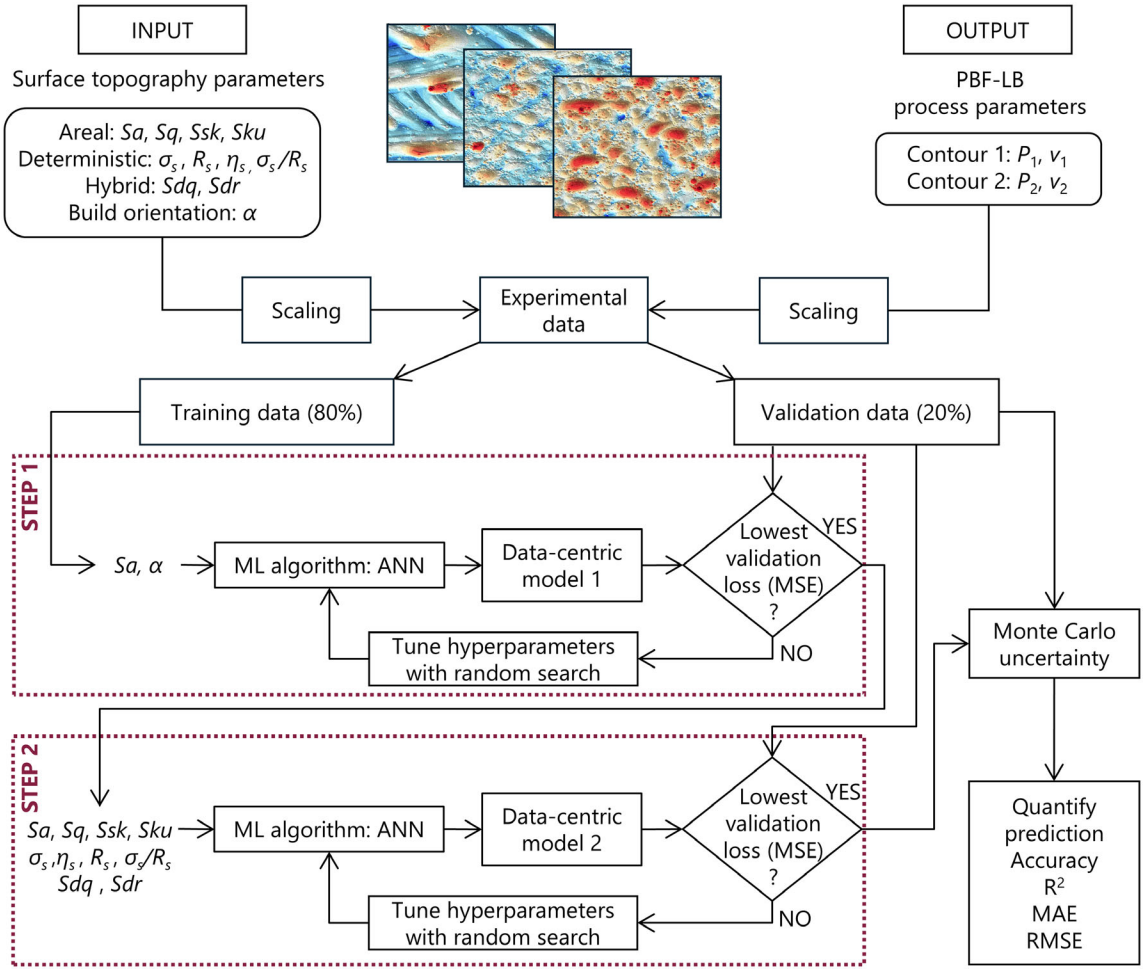

Figure 4. Flowchart of the methodology to develop and validate inverse data-centric models that link the as-built surface roughness parameters (input) to the PBF-LB process parameters (output) in a two-step process; step 1 links a single *Sa* and α value to a set of ten surface roughness parameters. Step 2 links the ten surface roughness parameters to the PBF-LB process parameters.

including areal, deterministic, and hybrid parameters. This translates minimal user input into a comprehensive, high-fidelity description of the desired surface roughness.

In step 2, a second ANN-based model (data-centric model 2 in Figure 4) uses the predicted surface roughness parameters of step 1 as input to predict the PBF-LB process parameters: P_1, v_1, P_2, v_2, and α. The hyperparameters of both ANNs are optimized using a random search to minimize the validation loss, which are calculated in terms of the mean squared error (MSE).[60] **Figure A1** (Appendix) shows the MSE as a function of time (epoch) to illustrate the learning rate of the inverse data-centric model in terms of both training and validation loss.

This two-step inverse modeling approach enables practical use of the model in a design and manufacturing context, where users are unlikely to know all ten surface roughness parameters. Instead, the model infers a complete surface roughness description from just *Sa* and α, and subsequently provides recommended PBF-LB process parameters.

However, to address the non-uniqueness of the inverse problem, i.e., many different surfaces may satisfy the same *Sa* value,[62] a Monte Carlo simulation approach is adopted. For each prediction, $N = 100$ iterations are performed, producing a distribution for each predicted process parameter.[63] The arithmetic mean of each distribution is used to calculate the prediction accuracy (R^2, MAE, and RMSE) of each model. Cases where the arithmetic mean <0 are discarded because those outcomes lack physical meaning. R^2, MAE, and RMSE reflect the cumulative prediction accuracy of steps 1 and 2. Additionally, for each data point in the validation set, the percent error of each PBF-LB process parameter (P_1, v_1, P_2, and v_2) is calculated, i.e., the ratio of the difference between the predicted and true value, and either the true value or the predicted value (based on the arithmetic mean of their respective distributions), whichever is larger. Finally, the arithmetic mean of the percent error over all four PBF-LB process parameters is computed and mapped as a function of combinations of *Sa* and α to visualize the prediction accuracy as a function of the surface roughness and build orientation.

Although inverse models using KNN, RF, SVR, and XGBoost algorithms are also developed, these models consistently underperform the models based on the ANN algorithm in terms of prediction accuracy. As in the forward modeling framework, the dataset is split randomly into 80% training data and 20% validation data to construct and evaluate the models, respectively. However, unlike the forward model, no cross-validation was used when developing the inverse model due to the significant computational cost.

3. Results and Discussion

3.1. Correlation Coefficient

Figure 5a depicts the Pearson linear correlation coefficients between the ten as-built surface roughness parameters and the PBF-LB process parameters. This analysis provides initial insight into potential linear relationships within the dataset. The deterministic and hybrid surface roughness parameters

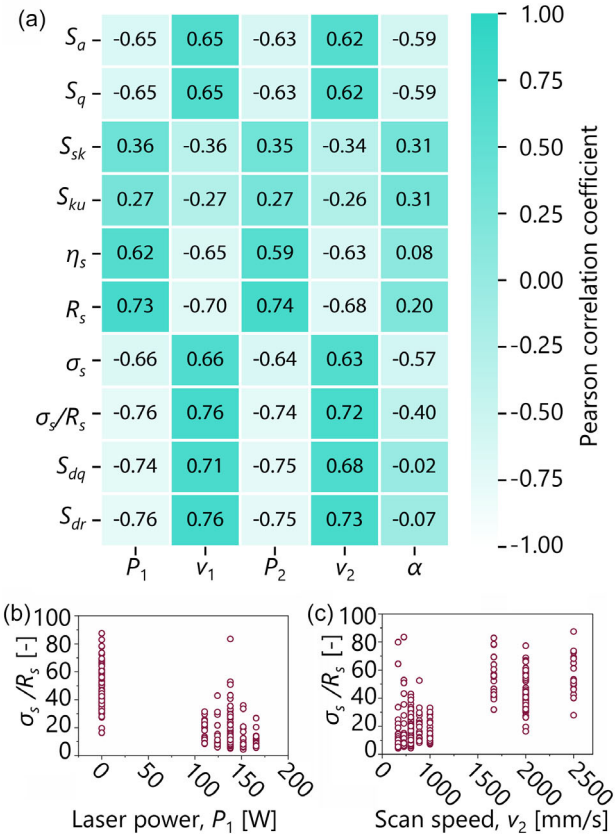

Figure 5. a) Pearson linear correlation coefficients between the as-built surface roughness parameters and the PBF-LB process parameters, and the deterministic roughness parameter as a function of b) the contour 1 laser power and c) the contour 2 laser scan speed to illustrate the ambiguous correlation between surface roughness and process parameters.

exhibit stronger linear correlations with the PBF-LB process parameters than the areal surface roughness parameters, consistent with previous studies.[12,33] This trend arises because deterministic and hybrid surface roughness parameters incorporate both height and spatial information of the surface roughness, whereas areal surface roughness parameters average height information over the entire as-built surface. However, despite its utility, a linear correlation coefficient alone is insufficient to characterize the complex relationship between PBF-LB process parameters and as-built surface roughness. Figure 5 also shows the deterministic roughness parameter σ_s/R_s as a function of the contour 1 laser power P_1 (Figure 5b) and the contour 2 laser scan speed v_2 (Figure 5c), respectively, to illustrate their non-unique relationship. This result emphasizes the limitations of linear correlation analysis for such complex relationships. Hence, one must consider non-linear relationships between the PBF-LB process parameters and the as-built surface roughness parameters.

3.2. Prediction Accuracy of the Forward Data-Centric Model

Table 2 presents the prediction accuracy metrics (R^2, MAE, and RMSE) for each of the 50 forward data-centric models. Each

Table 2. Prediction accuracy (R^2, MAE, RMSE) of the 50 forward data-centric models based on five different ML algorithms for each of ten surface roughness parameters.

	As-built surface roughness parameters	Metric	KNN	ANN	RF	SVR	XGBoost
Areal	Average surface roughness, *Sa*	R^2	0.815	0.866	**0.900**	0.709	0.879
		MAE	0.074	0.064	0.063	0.092	0.066
		RMSE	0.120	0.102	0.088	0.150	0.097
	RMS roughness, *Sq*	R^2	0.833	0.834	0.904	0.732	**0.907**
		MAE	0.073	0.073	0.065	0.090	0.059
		RMSE	0.117	0.116	0.088	0.1486	0.087
	Skewness, *Ssk*	R^2	0.315	0.249	**0.369**	0.323	0.212
		MAE	0.102	0.104	0.098	0.102	0.101
		RMSE	0.142	0.149	0.136	0.141	0.152
	Kurtosis, *Sku*	R^2	0.040	**0.046**	0.018	-0.005	0.003
		MAE	0.139	0.133	0.148	0.140	0.141
		RMSE	0.198	0.197	0.204	0.202	0.202
Deterministic	Standard deviation of summit heights, σ_s	R^2	0.836	0.754	**0.924**	0.740	0.907
		MAE	0.074	0.087	0.061	0.092	0.062
		RMSE	0.117	0.144	0.080	0.148	0.088
	Mean summit radius, R_s	R^2	0.800	0.754	**0.890**	0.790	0.859
		MAE	0.083	0.087	0.066	0.090	0.074
		RMSE	0.122	0.144	0.091	0.125	0.103
	Summit density, η_s	R^2	0.828	0.745	**0.902**	0.766	0.885
		RMSE	0.103	0.126	0.078	0.121	0.085
		MAE	0.074	0.095	0.062	0.099	0.063
	Roughness parameter, σ_s/R_s	R^2	0.856	0.781	0.924	0.808	**0.940**
		MAE	0.067	0.079	0.054	0.084	0.050
		RMSE	0.104	0.129	0.075	0.120	0.067
Hybrid	Root means square surface slope, *Sdq*	R^2	0.763	0.715	0.838	0.686	**0.896**
		MAE	0.093	0.109	0.076	0.105	0.064
		RMSE	0.131	0.144	0.109	0.151	0.087
	Developed interfacial area ratio, *Sdr*	R^2	0.784	0.706	**0.904**	0.637	0.891
		MAE	0.083	0.090	0.059	0.106	0.064
		RMSE	0.122	0.142	0.081	0.158	0.086

model represents a combination of one of five ML algorithms with one of ten surface roughness parameters. The models with the highest prediction accuracy (max. R^2, min. MAE, min. RMSE) for each surface roughness parameter are bolded. From Table 2, it is observed that the models with the highest prediction accuracy predominantly use RF (6 out of 10 surface roughness parameters), XGBoost (3 out of 10), and ANN (1 out of 10) algorithms. Table 2 also shows that the models perform worst for predicting the skewness *Ssk* and kurtosis *Sku*. The highest prediction accuracy is achieved for the deterministic and hybrid surface roughness parameters. This is consistent with the understanding that these surface roughness parameters incorporate surface height and spatial information, providing a more comprehensive representation of the as-built surface roughness and features that result from the PBF-LB process, in contrast to areal surface roughness parameters, which primarily average height information. The optimal hyperparameter combinations for the highest performing models, as well as their computation time for training, are provided in **Table A1**,**A2**, respectively (Appendix).

The Friedman test indicates that statistically significant differences exist between the prediction accuracy of the different forward data-centric models ($p < 0.05$) for all but one surface roughness parameter (*Sku*). The Nemenyi test subsequently shows that the prediction accuracy of the SVR-based model consistently underperforms the models based on the RF and XGBoost algorithms, whereas the models based on RF and XGBoost algorithms display similar prediction accuracy without a significant difference between them. **Table A3** summarizes the statistical analysis (Appendix).

Figure 6 validates the highest-performing forward data-centric models for each surface roughness parameter category: (a) areal, (b) deterministic, and (c) hybrid surface roughness parameters (see Table 2), using the 20% hold-out validation data. Each

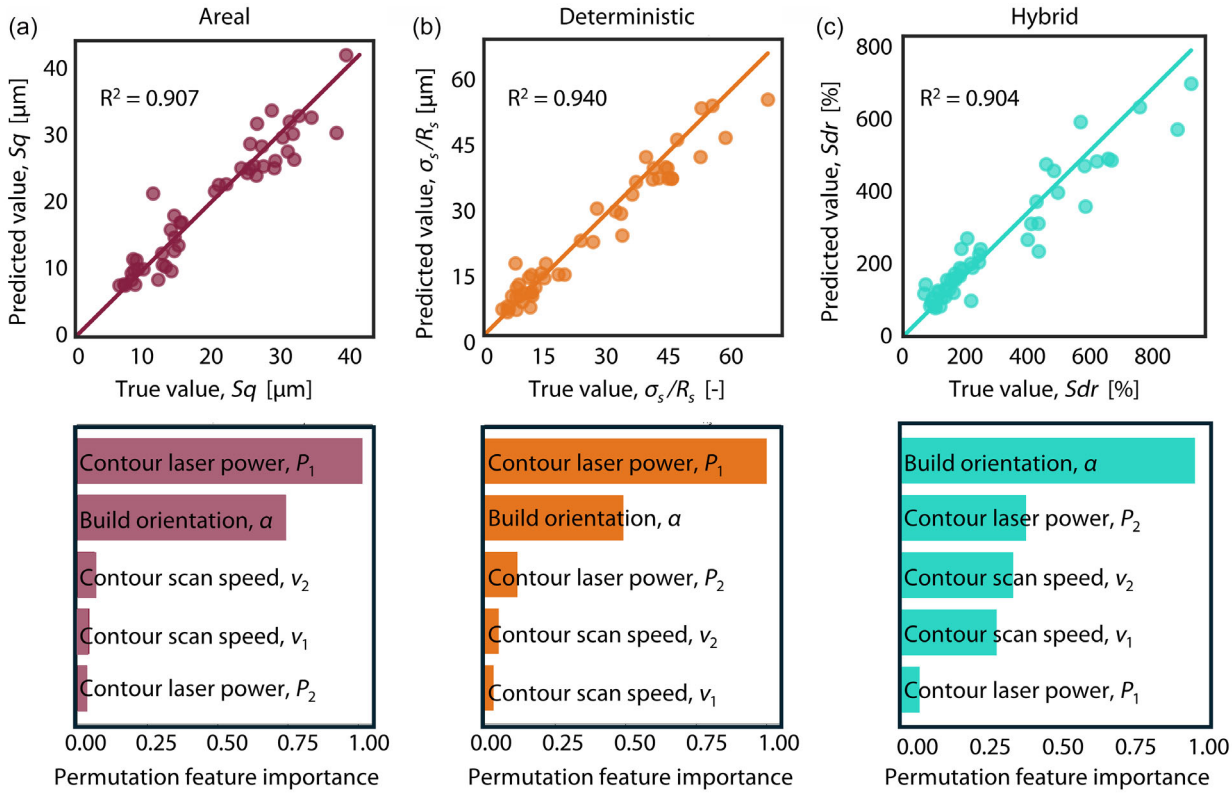

Figure 6. Experimental validation of the forward data-centric models with the highest prediction accuracy for a) areal, b) deterministic, and c) hybrid surface roughness parameters, using the validation dataset. The permutation feature importance identifies the relative effect of each input parameter in the prediction of the output parameters.

datapoint in Figure 6a–c shows the prediction of the surface roughness parameter using the forward data-centric model with PBF-LB process parameters from the validation data as input, compared to the corresponding ground-truth measurements (from validation data). The limited scatter of data points around the 45° line (indicating perfect prediction) confirms the strong prediction accuracy ($R^2 > 0.900$).

Additionally, permutation feature importance[64] is computed for each model to quantify the relative importance of each PBF-LB process parameter (input) in the prediction of the surface roughness parameter (output). The results demonstrate that the contour laser power and build orientation are the most influential parameters affecting the as-built surface roughness, consistent with prior studies (see, e.g.,).[12,33,41,46,47]

Quantifying the effect of PBF-LB process parameters on the as-built surface roughness parameters through physical experimentation is time-consuming and resource-intensive. However, such insights are critical for tuning PBF-LB process parameters to fabricate surfaces with tailored surface roughness and minimize the need for post-processing. The forward data-centric models provide a computational framework to visualize and analyze these relationships across the full process envelope. To illustrate this, **Figure 7** maps the predicted deterministic roughness parameter σ_s/R_s (highest prediction accuracy) as a function of the two most influential PBF-LB process parameters P_1 and α (see permutation feature importance, Figure 6). Inset images display experimentally measured surface roughness maps for selected specimens fabricated with different process parameters, including double (specimens 12, 8, and 4, $P_1 \neq 0$ W and $P_2 \neq 0$ W) and single (specimen 2, $P_1 = 0$ W and $P_2 \neq 0$ W) contour laser passes, and various build orientations ($\alpha = 0°$, 5°, 55°, and 85°). All images are rendered using a consistent color scale.

The predicted σ_s/R_s values range between ≈4 and 68, capturing the wide variability in surface roughness that results from different PBF-LB process parameters. The smoothest as-built surfaces correspond to horizontal build orientations ($\alpha = 0°$), regardless of P_1, as these surfaces do not display any staircase effect (a geometric artifact of the layer-wise approximation of inclined surfaces, see inset image 1) that dominates the as-built surface roughness for shallow build orientations (see inset image 6). This observation agrees with multiple experimental findings reported in the literature (e.g.,[12,13]).

Additionally, steep build orientation ($\alpha > 55°$) combined with high contour power ($P_1 > 120$ W) also yields smooth as-built surface roughness (see inset image 2). This is because overlapping contour scan lines at steep orientations smoothen the discrete layer steps. Notably, the required P_1 to obtain smooth as-built surfaces decreases with increasing $\alpha > 55°$, as fewer discrete steps need to be melted over and a smaller melt pool can smoothen those surface features (see inset

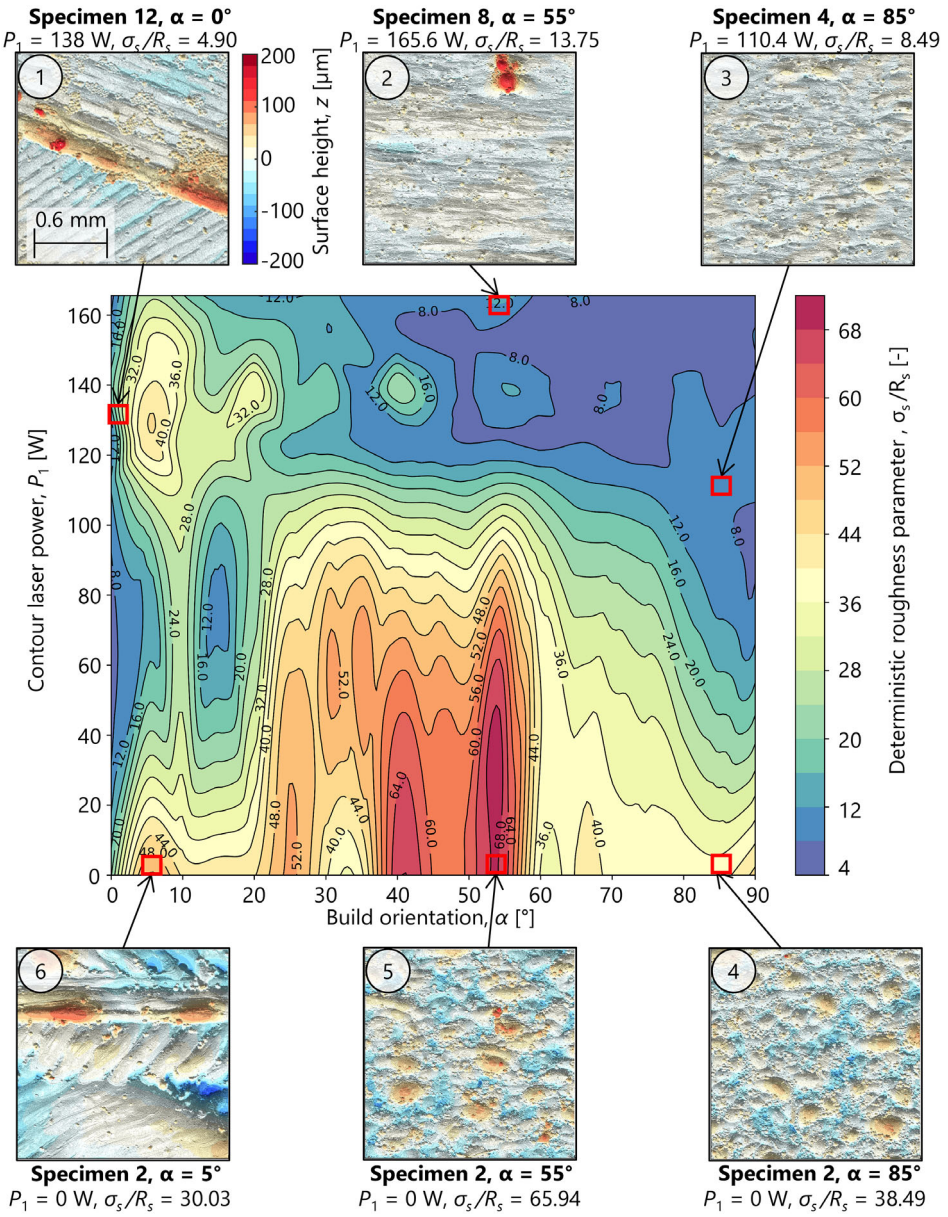

Figure 7. Deterministic roughness parameter σ_s/R_s as a function of build orientation α and contour laser power P_1. Inset images show experimental surface roughness maps of selected as-built surfaces fabricated with double (specimens 4, 8, and 12) and single (specimen 2) contour laser passes. All inset images scale according to the same color bar as the inset image 1.

image 3). This result agrees with experimental work published by others.[12,65]

Conversely, σ_s/R_s increases with decreasing P_1, regardless of α. This is especially pronounced for intermediate build orientations $5° \leq \alpha \leq 55°$, where either a shallow build orientation (staircase effect) prevents the contour laser pass to cover the interior hatching and, thereby, creates coarse as-built surfaces (see inset image 6), or an intermediate build orientation with insufficient power P_1 to smoothen the discrete steps between subsequent layers results in balling phenomena between layers (see inset images 4 and 5), also noted in prior work.[12]

Hence, Figure 7 demonstrates that data-centric models can efficiently map the complex relationship between PBF-LB process parameters and as-built surface roughness across the entire process envelope. An insight that would be prohibitively expensive and time-consuming to acquire through experiments only.

3.3. Prediction Accuracy of the Inverse Data-Centric Model

Table 3 summarizes the prediction accuracy (R^2, MAE, and RMSE) of the inverse data-centric model. This model predicts the distribution of PBF-LB process parameters based on the

Table 3. Prediction accuracy (R^2, MAE, RMSE) of the PBF-LB process parameters that result from the inverse data-centric model.

PBF-LB process parameters	R^2	MAE	RMSE
Contour 1 laser power P_1	0.832	0.097	0.171
Contour 1 laser scan speed v_1	0.838	0.098	0.191
Contour 2 laser power P_2	0.786	0.112	0.158
Contour 2 laser scan speed v_2	0.790	0.107	0.156

Table 4. Experimental validation of an inverse data-centric model for a typical example, showing the predicted and true values for all PBF-LB process parameters for $Sa = 20.07\,\mu m$ and $\alpha = 15°$ as input.

PBF-LB process parameters	Predicted	True	Difference [%]
Contour 1 laser power P_1	137.55 W	138.00 W	0.32
Contour 1 laser scan speed v_1	381.12 mm s^{-1}	390.00 mm s^{-1}	2.30
Contour 2 laser power P_2	79.11 W	80.00 W	1.11
Contour 2 laser scan speed v_2	740.07 mm s^{-1}	800.00 mm s^{-1}	7.78

desired as-built surface roughness parameters and build orientation. The prediction accuracy is calculated using the arithmetic mean of the predicted distribution of each PBF-LB process parameter (see Section 2.4.2). From Table 3, the highest prediction accuracy occurs for P_1 and v_1, although it is similar for all four PBF-LB process parameters.

Figure 8 validates the inverse data-centric model for the PBF-LB process parameters; (a) P_1 (b) v_1 (c) P_2, and (d) v_2, using the 20% hold-out validation data. Each data point in Figure 8a–d shows the arithmetic mean of the predicted distribution of the process parameter using the inverse data-centric model from the validation data as input, compared to the corresponding ground-truth (from validation data). The modest scatter of data points around the around the 45° line (indicating perfect prediction) confirms the strong prediction accuracy ($R^2 \approx 0.81$).

To demonstrate the practical utility of the inverse model, a representative use case is illustrated; predicting the PBF-LB process parameters to achieve a desired as-built surface roughness of $Sa = 20.07\,\mu m$ at a build orientation $\alpha = 15°$. **Figure 9**a–d shows the predicted distributions of the different PBF-LB process parameters that result from the inverse model. Additionally, **Table 4** summarizes the predicted arithmetic means and true values of the PBF-LB process parameter. The variation between the prediction and true value is within 8% for all PBF-LB process parameters.

To assess the generalizability of the inverse model across the entire process envelope, **Figure 10** presents the mean percent error of the predicted PBF-LB process parameters as a function of Sa and α. For each validation data point, the percent error is computed for each of the four predicted PBF-LB process

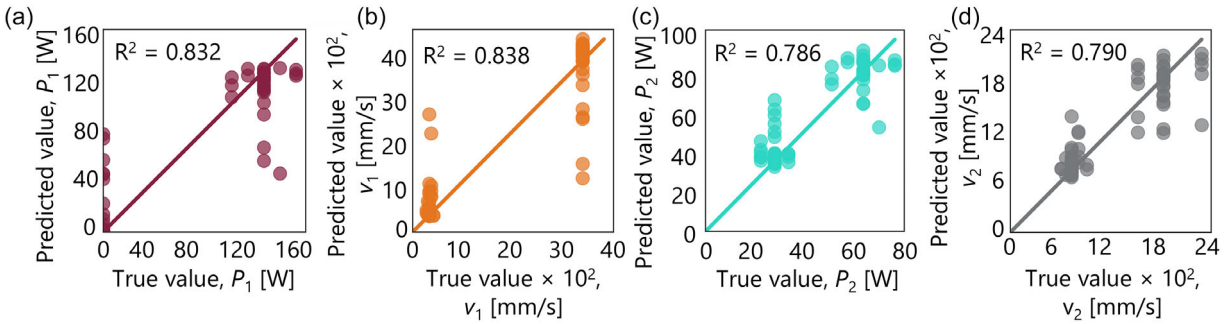

Figure 8. Experimental validation of the inverse data-centric model, showing the prediction accuracy for all PBF-LB process parameters: a) P_1, b) v_1, c) P_2, and d) v_2, using the validation data.

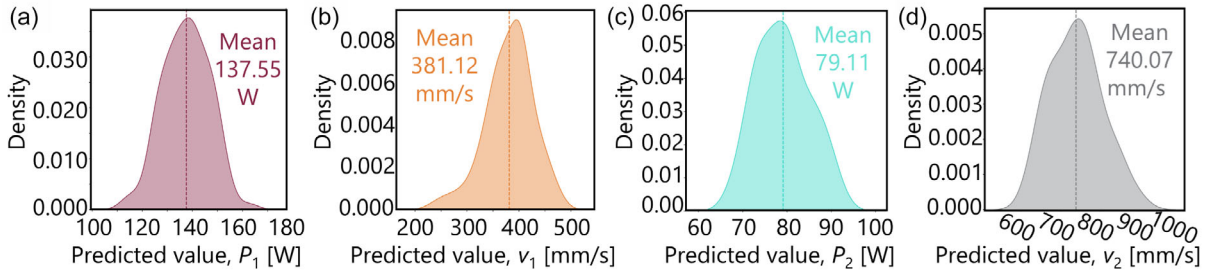

Figure 9. Experimental validation of inverse data-centric model for a typical example, showing the distribution for all PBF-LB process parameters: a) P_1, b) v_1, c) P_2, and d) v_2, for $Sa = 20.07\,\mu m$ and $\alpha = 15°$ as input.

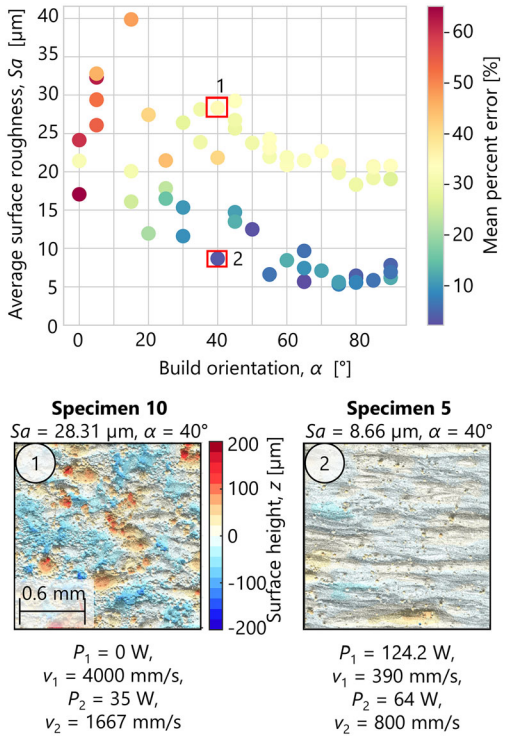

Figure 10. Mean percent error of the inverse model as a function of build orientation α and average surface roughness *Sa*. Inset images show experimental surface roughness maps of selected as-built surfaces representing typical examples of high and low mean percent error.

parameters (P_1, v_1, P_2, and v_2) as the difference between the prediction and the true value, divided by the true value (based on the arithmetic mean of their respective distributions). The arithmetic mean of the percent error of the four PBF-LB process parameter predictions is reported.

Figure 10 shows that the mean percent error decreases with increasing build orientation α and with decreasing surface roughness *Sa*. The prediction error is lowest for shallow build orientations ($\alpha < 15°$), where the surface roughness is dominated by the interior hatch pattern and the staircase effect, which results from the stepped approximation of inclined geometries in layer-wise fabrication.[12] The average roughness *Sa* does not accurately capture (local) surface features such as the staircase effect, because it averages all surface heights over the entire surface. For increasing build orientations, the contour laser pass increasingly mitigates these effects, and the prediction accuracy of the model increases.

However, when $\alpha > 15°$, variability of the prediction accuracy re-emerges. Specimens fabricated with a single contour laser pass ($P_1 = 0$ W, see inset image 1) exhibit coarser surface roughness than those fabricated with two contour laser passes (see inset image 2). The second contour laser pass provides additional smoothening in addition to the first contour laser pass and, thus, reduces *Sa*. Consequently, the model achieves higher accuracy when predicting smoother surfaces, where the spatial variability is lower, and *Sa* provides a more representative measure of surface roughness.

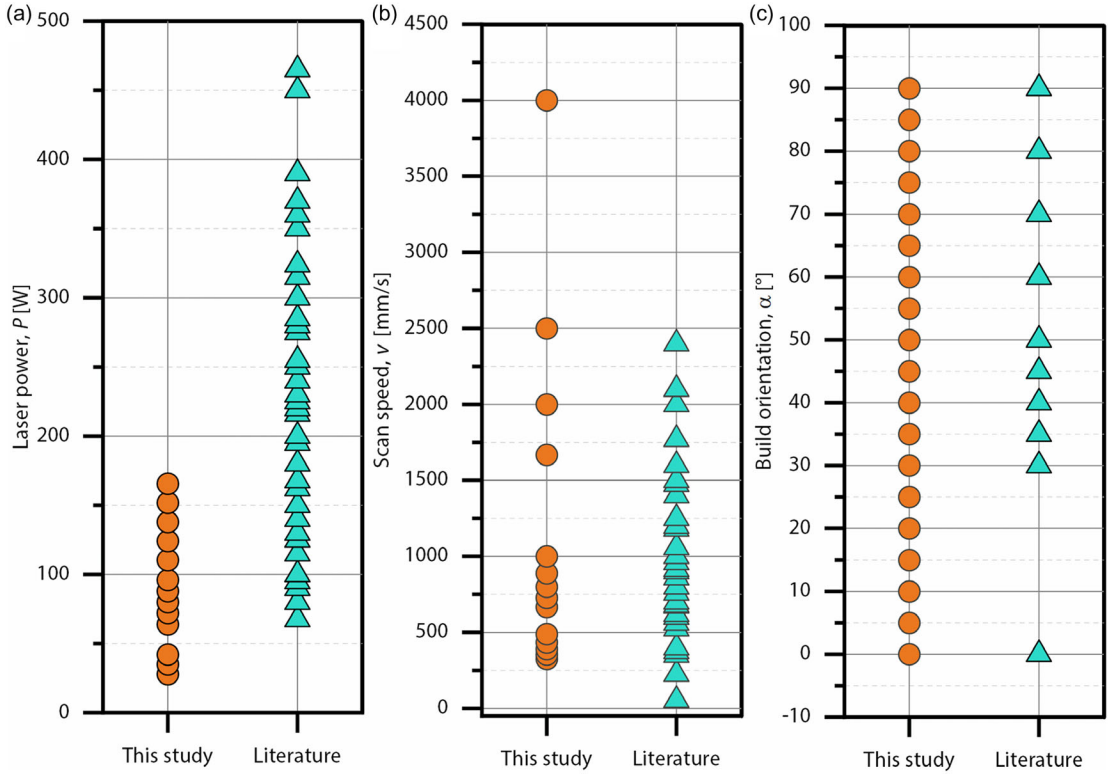

Figure 11. Comparison between the range of the PBF-LB process parameters for IN718 used in this work (orange circles) and those documented in the literature (green triangles), including a) laser power, b) laser scan speed, and c) build orientation.

3.4. Limitations

The prediction accuracy of data-centric models is fundamentally tied to the size and scope of the experimental dataset used to derive them. **Figure 11** compares the process envelope of the PBF-LB process parameters considered in this work (orange circles) with those reported in the literature IN718 (green triangles), including (a) laser power, (b) laser scan speed, and (c) build orientation. From Figure 11, it is evident that our dataset spans nearly the full range of reported values for laser scan speed and build orientation, thus ensuring that the derived models generalize well across typical PBF-LB conditions for IN718. However, a few studies report higher laser power values than those used in this study, for instance, in applications that involve multi-material processing (e.g., fuse IN718 with 316 stainless steel) or to tailor the microstructure and crystallographic texture of fabricated parts.[66,67] Expanding the process envelope to include such high-power regimes, along with additional experimental data, would likely increase the prediction accuracy of both forward and inverse data-centric models.

The prediction accuracy of the inverse model (≈80%) is slightly lower than that of the forward model (≈90%). This is primarily due to the two-step architecture of the inverse modeling approach; step 1 predicts the full set of surface roughness parameters from a given average surface roughness Sa and build orientation α, whereas step 2 maps these predicted surface roughness parameters to the corresponding PBF-LB process parameters. Each step introduces its own prediction error, and because these are executed in series, the compounded uncertainty reduces the overall prediction accuracy of the inverse model relative to the single-step forward model.

Additionally, the two-step inverse modeling approach adds considerable computational cost compared to the forward model, which precludes the use of tenfold cross-validation during training of the inverse model. A potential solution could be to use a multi-output ensemble model that simultaneously predicts multiple process parameters. However, such models require larger experimental datasets to avoid overfitting.

Another promising strategy to improve prediction accuracy while reducing data requirements is to incorporate physics-informed ML (PIML). By embedding physical constraints and domain knowledge directly into the model structure or loss function, PIML leverages smaller datasets to improve model interpretability. For example, known relationships between melt pool behavior, heat transfer, and surface roughness could guide the model architecture or inform feature engineering.

Finally, although the forward and inverse modeling frameworks presented in this work are general and not limited to a specific material system or AM modality, the specific results relating process parameters to surface roughness (and vice versa) are applicable only to IN718. This limitation arises from the fact that all experimental data used in this study were obtained from IN718 specimens. Nevertheless, the modeling framework itself can be applied to other materials, provided that appropriate experimental data are available, enabling practitioners to gain material-specific insights into the process–surface roughness relationship.

4. Conclusion

A data-centric modeling framework to quantitatively establish the relationships between PBF-LB process parameters and as-built surface roughness parameters for IN718 specimens is presented, spanning the full process envelope. This framework enables both forward prediction and inverse design of process parameters, offering new capabilities to optimize surface roughness in PBF-LB without extensive post-processing.

A forward data-centric model that maps PBF-LB process parameters to a comprehensive set of areal and deterministic as-built surface roughness parameters is developed and implemented. Models based on the deterministic roughness parameter σ_s/R_s, which capture both spatial and height information of the as-built surface roughness, yield the highest prediction accuracy (≈90%). This highlights the importance of integrating spatial information, in addition to height information, to effectively model the complex surface features of the as-built surfaces, intrinsic to layer-wise fabrication.

The forward data-centric model enables quantitative mapping of the effect of the PBF-LB process parameters on the as-built surface roughness, providing a fast and scalable alternative to time-consuming experimental trial-and-error. In doing so, the model not only supports process tuning for desired surface roughness but also offers physics-informed insights into the underlying process-surface relationships in PBF-LB. This capability is essential for intelligent PBF-LB systems aimed at real-time process optimization and in-situ control.

An inverse data-centric model is introduced for the first time, which infers a distribution of PBF-LB process parameters from a desired average roughness and build orientation. The two-step model reconstructs a full set of surface roughness parameters and then maps them to process parameters. Despite its computational cost, the inverse model achieves a prediction accuracy of ≈80%, enabling process parameter selection to meet surface roughness specifications without post-processing. This capability is critical for adaptive AM workflows and closed-loop control systems where reverse mapping from desired outcomes to process inputs is essential.

Together, the forward and inverse data-centric models form a complementary framework that supports intelligent decision-making in PBF-LB. Expanding the experimental dataset, integrating PIMS, and developing ensemble or multi-output architectures could further enhance model efficiency, as well as generalizability across alloys, geometries, and machine platforms.

An online tool that implements the forward and inverse models of this work is available at https://amsurfaces.cs.vt.edu/ for readers to explore.

Appendix

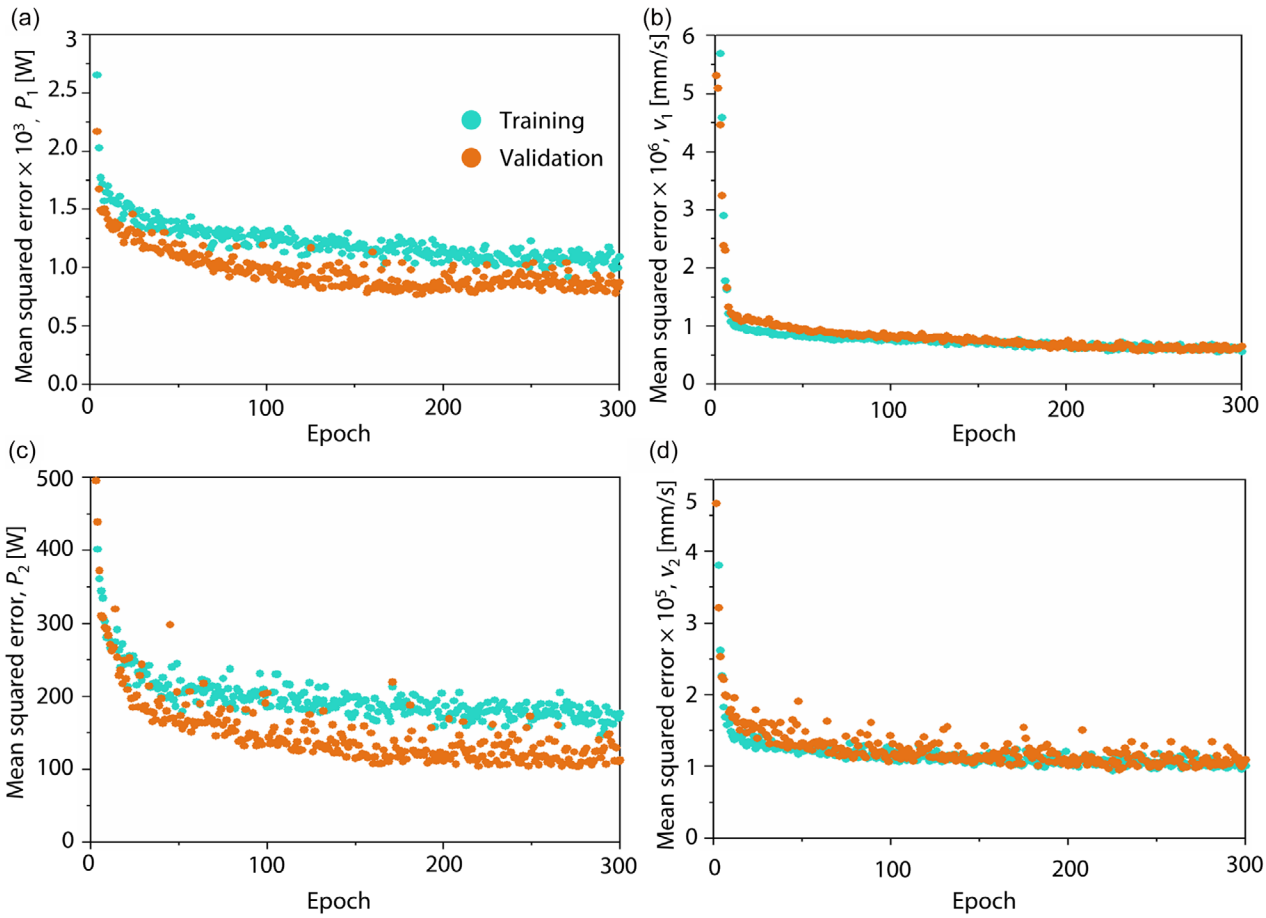

Figure A1. MSE as a function of time (epoch) to illustrate the learning rate of the inverse data-centric model in terms of both training and validation loss to predict each PBF-LB process parameters: a) $P1$, b) v_1, c) P_2, and d) v_2.

Table A1. Hyperparameter range for grid search using the forward model and hyperparameters to achieve the highest prediction accuracy for each of 10 surface roughness parameters.

Surface topography parameters	Hyperparameter range	Hyperparameters for achieving the highest prediction accuracy
Sa	(RF)	Bootstrap True, max. depth 20, min. samples leaf 1, min. samples split 2, *N* estimators 100
σ_s	*N* estimators 100, 200, 300	Bootstrap True, max. depth 20, min. samples leaf 1, min. samples split 2, *N* estimators 100
R_s	Max. depth 10, 20, 30, none	Bootstrap True, max depth 20, min samples leaf 1, min. samples split 2, *N* estimators 100
η_s	Min. samples split 2,5,10	Bootstrap True, max depth 20, min samples leaf 1, min. samples split 5, *N* estimators 100
Sdr	Min. samples leaf 1,2,4	Bootstrap True, max. depth 10, min. samples leaf 1, min. samples split 2, *N* estimators 300
Sq	Bootstrap True, False	Colsample bytree 1.0, gamma 0.1, learning rate 0.1, max. depth 3, *N* estimator 300, subsample 0.8
σ_s/R_s	(XGBoost)	Colsample bytree 1.0, gamma 0.3, learning rate 0.2, max. depth 3, *N* estimator 200, subsample 0.8
Sdq	*N* estimator 100, 200, 300	Colsample bytree 0.8, gamma 0.1, learning rate 0.01, max. depth 5, *N* estimator 300, subsample 0.8
	Max. depth 3,5,7	
	Learning rate 0.01, 0.1, 0.2	
	Subsample 0.8 1.0	
	Colsample bytree 0.8, 1.0	
	Gamma 0,0.1,0.3	

Table A2. Computation time for training the forward model using five different ML algorithms for predicting the deterministic roughness parameter(σ_s/R_s).

Model	Test-train split	R^2 [σ_s/R_s]	Computation time [min]
XGBoost	80–20	0.94	3.29
RF	80–20	0.92	9.48
SVR	80–20	0.81	0.32
KNN	80–20	0.86	0.80
ANN	80–20	0.78	105. 80

Table A3. Statistical comparison of the prediction accuracy of the different forward data-centric models using the Friedman test and Nemenyi post-hoc test.

	As-built surface roughness parameters	Friedman test p-value	Statistically significant? ($p < 0.05$)	Pairwise significant differences (Nemenyi test, $p < 0.05$)
Areal	*Sa*	0.0026	Yes	SVR < RF ($p = 0.008$), SVR < XGBoost ($p = 0.022$)
	Sq	0.0027	Yes	SVR < RF ($p = 0.0166$), SVR < XGBoost ($p = 0.040$), ANN < RF ($p = 0.040$)
	Ssk	0.0110	Yes	ANN < XGBoost ($p = 0.006$)
	Sku	0.0648	No	–
Deterministic	σ_s	0.0014	Yes	SVR < RF ($p = 0.006$), SVR < XGBoost ($p = 0.011$)
	R_s	0.0007	Yes	SVR < RF ($p = 0.001$), SVR < XGBoost $p = (0.040)$, ANN < XGBoost ($p = 0.011$)
	η_s	0.0017	Yes	SVR < RF ($p = 0.008$), SVR < XGBoost ($p = 0.022$)
	σ_s/R_s	0.0010	Yes	SVR < RF ($p = 0.030$), SVR < XGBoost ($p = 0.002$), ANN < XGBoost ($p = 0.023$)
Hybrid	*Sdq*	0.0011	Yes	SVR < RF ($p = 0.040$), SVR < XGBoost ($p = 0.002$), ANN < XGBoost ($p = 0.023$)
	Sdr	0.0010	Yes	SVR <RF ($p = 0.003$), SVR <XGBoost ($p = 0.031$), ANN <RF ($p = 0.023$)

Acknowledgements

The authors acknowledge support from the National Science Foundation award CNS-2328112 and the Department of Defense, Office of Local Defense Community Cooperation award DD2064-23-01. The authors also thank the following Virginia Tech undergraduate computer science students who implemented the online tool (https://amsurfaces.cs.vt.edu/) as part of their capstone CS 4704 course: Daniel Jagga, Camden Johnson, Trevor Jarzynka, and Dominic Martin.

Conflict of Interest

The authors declare no conflict of interest

Author Contributions

Samsul Mahmood: conceptualization (equal); data curation (lead); formal analysis (lead); methodology (equal); validation (lead); visualization (equal); writing—original draft (lead). **Bart Raeymaekers**: conceptualization (equal); funding acquisition (lead); methodology (equal); supervision (lead); validation (equal); visualization (lead); writing—review and editing (lead).

Data Availability Statement

The data that support the findings of this study are available from the corresponding author upon reasonable request.

Keywords

Inconel 718, inverse model, laser powder bed fusion, machine learning, surface roughness

Received: April 10, 2025
Revised: July 27, 2025
Published online:

[1] I. Gibson, D. Rosen, B. Stucker, *Additive Manufacturing Technologies: 3D Printing, Rapid Prototyping, and Direct Digital Manufacturing*, Springer, New York, NY **2015**.
[2] B. Blakey-Milner, P. Gradl, G. Snedden, M. Brooks, J. Pitot, E. Lopez, M. Leary, F. Berto, A. Du Plessis, *Mater. Des.* **2021**, *209*, 110008.
[3] F. Kerstens, A. Cervone, P. Gradl, *Acta Astronaut.* **2021**, *182*, 454.
[4] S. Chowdhury, N. Yadaiah, C. Prakash, S. Ramakrishna, S. Dixit, L. R. Gupta, D. Buddhi, *J. Mater. Res. Technol.* **2022**, *20*, 2109.
[5] J. C. Snyder, K. A. Thole, *J. Turbomachinery* **2020**, *142*, 051007.
[6] M. Javaid, A. Haleem, *Alexandria J. Med.* **2018**, *54*, 411.
[7] L. E. Murr, S. M. Gaytan, F. Medina, H. Lopez, E. Martinez, B. I. Machado, D. H. Hernandez, L. Martinez, M. I. Lopez, R. B. Wicker, J. Bracke, *Phil. Trans. Royal Soc. A* **2010**, *368*, 1999.
[8] A. J. Sheoran, H. Kumar, P. K. Arora, G. Moona, *Proc. Manuf.* **2020**, *51*, 663.
[9] S. Singh, S. Ramakrishna, *Curr. Opin. Biomed. Eng.* **2017**, *2*, 105.
[10] J. C. Vasco, *Additive Manufacturing*, Elsevier, Amsterdam, New York **2021**, pp. 505–530.
[11] R. Leal, F. M. Barreiros, L. Alves, F. Romeiro, J. C. Vasco, C. Marto, *Int. J. Adv. Manuf. Technol.* **2017**, *92*, 1671.
[12] B. Raeymaekers, T. Berfield, *Rapid Prototyping J.* **2024**, *31*, 200.
[13] G. Strano, L. Hao, R. M. Everson, K. E. Evans, *J. Mater. Process. Technol.* **2013**, *213*, 589.
[14] D. S. Watring, K. C. Carter, D. Crouse, B. Raeymaekers, A. D. Spear, *Mater. Sci. Eng.: A* **2019**, *761*, 137993.
[15] J. Gockel, L. Sheridan, B. Koerper, B. Whip, *Int. J. Fatigue* **2019**, *124*, 380.
[16] S. Lee, B. Rasoolian, D. F. Silva, J. W. Pegues, N. Shamsaei, *Addit. Manuf.* **2021**, *46*, 102094.
[17] J. Elambasseril, J. Rogers, C. Wallbrink, D. Munk, M. Leary, M. Qian, *Crit. Rev. Solid State Mater. Sci.* **2023**, *48*, 132.
[18] J. H. Martin, B. D. Yahata, J. M. Hundley, J. A. Mayer, T. A. Schaedler, T. M. Pollock, *Nature* **2017**, *549*, 365.
[19] R. Ghanavati, E. Lannunziata, E. Norouzi, S. Bagherifard, L. Iuliano, A. Saboori, *Mater. Lett.* **2023**, *349*, 134793.
[20] M. Balbaa, S. Mekhiel, M. Elbestawi, J. McIsaac, *Mater. Des.* **2020**, *193*, 108818.
[21] K. Nakayama, H. Hashimoto, *Wear* **1995**, *185*, 173.

[22] N. N. Kumbhar, A. V. Mulay, *J. Inst. Eng. India Ser. C* **2018**, *99*, 481.
[23] J. Xu, T. Ma, R. L. Peng, S. Hosseini, *Addit. Manuf.* **2021**, *48*, 102416.
[24] W. Tillmann, C. Schaak, J. Nellesen, M. Schaper, M. E. Aydinöz, K.-P. Hoyer, *Addit. Manuf.* **2017**, *13*, 93.
[25] D. A. Lesyk, S. Martinez, B. N. Mordyuk, V. V. Dzhemelinskyi, A. Lamikiz, G. I. Prokopenko, *Surf. Coat. Technol.* **2020**, *381*, 125136.
[26] D. J. Newell, R. P. O'Hara, G. R. Cobb, A. N. Palazotto, M. M. Kirka, L. W. Burggraf, J. A. Hess, *Mater. Sci. Eng.: A* **2019**, *764*, 138230.
[27] N. Mohammadian, S. Turenne, V. Brailovski, *J. Mater. Process. Technol.* **2018**, *252*, 728.
[28] D. A. Lesyk, V. V. Dzhemelinskyi, S. Martinez, B. N. Mordyuk, A. Lamikiz, *J. Mater. Eng. Perform.* **2021**, *30*, 6982.
[29] T. Klotz, D. Delbergue, P. Bocher, M. Lévesque, M. Brochu, *Int. J. Fatigue* **2018**, *110*, 10.
[30] C. Guo, S. Li, S. Shi, X. Li, X. Hu, Q. Zhu, R. M. Ward, *J. Mater. Process. Technol.* **2020**, *285*, 116788.
[31] T. Yang, T. Liu, W. Liao, E. MacDonald, H. Wei, X. Chen, L. Jiang, *J. Mater. Process. Technol.* **2019**, *266*, 26.
[32] H. Hassanin, M. A. El-Sayed, M. Ahmadein, N. A. Alsaleh, S. Ataya, M. M. Z. Ahmed, K. Essa, *Micromachines* **2023**, *14*, 1642.
[33] S. Detwiler, D. Watring, A. Spear, B. Raeymaekers, *Precis. Eng.* **2022**, *74*, 303.
[34] International organization for standardization, Geometric product specifications (GPS)-surface texture : Profile, ISO 21920, **2021**.
[35] International organization for standardization, Geometrical product specifications (GPS) — Surface texture: Areal, ISO 25178, **2021**.
[36] M. Kalin, A. Pogačnik, I. Etsion, B. Raeymaekers, *Tribol. Int.* **2016**, *93*, 137.
[37] G. Pawar, P. Pawlus, I. Etsion, B. Raeymaekers, *J. Tribol.* **2013**, *135*, 011401.
[38] S. Detwiler, B. Raeymaekers, *J. Tribol.* **2022**, *144*, 121703.
[39] W. Muhammad, J. Ksang, O. Ibragimova, K. Inal, *Weld World* **2023**, *67*, 897.
[40] N. D. Dejene, H. G. Lemu, E. M. Gutema, *Int. J. Adv. Manuf. Technol.* **2024**, *133*, 5611.
[41] A. Garg, J. S. L. Lam, M. M. Savalani, *J. Intell. Manuf.* **2018**, *29*, 1191.
[42] D. Yan, E. T. Lee, S. Pasebani, Z. Fan, *Manufacturing Equipment and Automation; Manufacturing Processes; Manufacturing Systems; Nano/Micro/Meso Manufacturing; Quality and Reliability*, Vol. *2*, American Society of Mechanical Engineers, New Brunswick, NJ **2023**.
[43] B. Fotovvati, S. Rauniyar, J. A. Arnold, K. Chou, *Int. J. Adv. Manuf. Technol.* **2022**, *123*, 119.
[44] T. Özel, A. Altay, B. Kaftanoğlu, R. Leach, N. Senin, A. Donmez, *J. Manuf. Sci. Eng.* **2020**, *142*, 011008.
[45] B. Fotovvati, M. Balasubramanian, E. Asadi, *Coatings* **2020**, *10*, 1104.
[46] J. Koo, S. Lee, A. M. C. Baek, E. Park, N. Kim, *3D Printing Addit. Manuf.* **2024**, *11*, 1510.
[47] H. S. Park, D. S. Nguyen, T. Le-Hong, X. Van Tran, *J. Intell. Manuf.* **2022**, *33*, 1843.
[48] S. Toorandaz, K. Taherkhani, F. Liravi, E. Toyserkani, *Addit. Manuf.* **2024**, *91*, 104354.
[49] U. Scipioni Bertoli, A. J. Wolfer, M. J. Matthews, J.-P. R. Delplanque, J. M. Schoenung, *Mater. Des.* **2017**, *113*, 331.
[50] Z. Gu, S. Sharma, D. A. Riley, M. V. Pantawane, S. S. Joshi, S. Fu, N. B. Dahotre, *J. Intell. Manuf.* **2023**, *34*, 3341.
[51] A. Senthilnathan, P. Acar, B. Raeymaekers, *Tribol. Lett.* **2023**, *71*, 85.
[52] J. Seo, P. Rao, B. Raeymaekers, *Friction* **2023**, *12*, 1283.
[53] L. Cao, J. Li, J. Hu, H. Liu, Y. Wu, Q. Zhou, *Opt. Laser Technol.* **2021**, *142*, 107246.
[54] B. Raeymaekers, F. E. Talke, *Wear* **2010**, *269*, 416.
[55] T. Huynh, A. Mehta, K. Graydon, J. Woo, S. Park, H. Hyer, L. Zhou, D. D. Imholte, N. E. Woolstenhulme, D. M. Wachs, Y. Sohn, *Metallogr., Microstruct., Anal.* **2022**, *11*, 88.
[56] C. U. Brown, G. Jacob, A. Possolo, C. Beauchamp, M. Peltz, M. Stoudt, A. Donmez, *The Effects of Laser Powder Bed Fusion Process Parameters on Material Hardness and Density for Nickel Alloy*, Vol. *625*, National Institute of Standards and Technology, Gaithersburg, MD **2018**, pp. 100–19.
[57] P. Pawlus, R. Reizer, M. Wieczorowski, *Materials* **2021**, *14*, 5326.
[58] D. Freeman, R. Pisani, R. Purves, *Statistics*, 4th ed., W.W. Norton and Co., New York, NY **2007**.
[59] A. Burkov, *Machine Learning Engineering*, True Positive Inc, Quebec City, Canada **2020**.
[60] K. Tyagi, C. Rane, M. Manry, *Artificial Intelligence and Machine Learning for EDGE Computing*, Elsevier, Amsterdam, New York **2022**, pp. 53–63.
[61] P. B. Nemenyi, *Ph.D. Thesis*, Princeton University, NJ, USA **1963**.
[62] C. M. Mate, *Tribology on the Small Scale*, Oxford University Press, Oxford, New York **2007**.
[63] D. Milanés-Hermosilla, R. Trujillo Codorniú, R. López-Baracaldo, R. Sagaró-Zamora, D. Delisle-Rodriguez, J. J. Villarejo-Mayor, J. R. Núñez-Álvarez, *Sensors* **2021**, *21*, 7241.
[64] A. Altmann, L. Toloşi, O. Sander, T. Lengauer, *Bioinformatics* **2010**, *26*, 1340.
[65] Q. Jia, D. Gu, *J. Alloys Compd.* **2014**, *585*, 713.
[66] O. Gokcekaya, T. Ishimoto, S. Hibino, J. Yasutomi, T. Narushima, T. Nakano, *Acta Mater.* **2021**, *212*, 116876.
[67] W.-Y. Chen, X. Zhang, M. Li, R. Xu, C. Zhao, T. Sun, *Addit. Manuf.* **2020**, *36*, 101500.